J. Plasma Phys. (2021), *vol*. 87, 905870618
Published by Cambridge University Press
doi:10.1017/S0022377821001215

Effect of ionization waves on dust chain formation in a DC discharge

L.S. Matthews [1,†], K. Vermillion [1], P. Hartmann [1,2], M. Rosenberg [3], S. Rostami [1], E.G. Kostadinova [1,4], T.W. Hyde [1], M.Y. Pustylnik [5], A.M. Lipaev [6,7], A.D. Usachev [6], A.V. Zobnin [6], M.H. Thoma [8], O.F. Petrov [1,6,7], H.M. Thomas [5] and O.V. Novitskiy [9]

[1]CASPER, Baylor University, One Bear Place 97316, Waco, TX 76798-7316, USA

[2]Institute for Solid State Physics and Optics, Wigner Research Centre for Physics, PO Box 49, H-1525 Budapest, Hungary

[3]Department of Electrical and Computer Engineering, University of California San Diego, La Jolla, CA 92093, USA

[4]Physics Department, Auburn University, Auburn, AL 36849, USA

[5]Institut für Materialphysik im Weltraum, Deutsches Zentrum für Luft- und Raumfahrt (DLR), Münchener Straße 20, 82234 Weßling, Germany

[6]Institute for High Temperatures, Russian Academy of Sciences, Izhorskaya 13/19, 125412 Moscow, Russia

[7]Moscow Institute of Physics and Technology, Institutsky Lane 9, Dolgoprudny, Moscow Region 141700, Russia

[8]I. Physikalisches Institut, Justus-Liebig-Universität Gießen, Heinrich-Buff-Ring 16, 35392 Gießen, Germany

[9]Gagarin Research and Test Cosmonaut Training Center, 141160 Star City, Moscow Region, Russia

(Received 22 July 2021; revised 4 November 2021; accepted 10 November 2021)

An interesting aspect of complex plasma is its ability to self-organize into a variety of structural configurations and undergo transitions between these states. A striking phenomenon is the isotropic-to-string transition observed in electrorheological complex plasma under the influence of a symmetric ion wake field. Such transitions have been investigated using the Plasma Kristall-4 (PK-4) microgravity laboratory on the International Space Station. Recent experiments and numerical simulations have shown that, under PK-4-relevant discharge conditions, the seemingly homogeneous direct current discharge column is highly inhomogeneous, with large axial electric field oscillations associated with ionization waves occurring on microsecond time scales. A multi-scale numerical model of the dust–plasma interactions is employed to investigate the role of the electric field in the charge of individual dust grains, the ion wake field and the order of string-like structures. Results are compared with those for dust strings formed in similar conditions in the PK-4 experiment.

† Email address for correspondence: lorin_matthews@baylor.edu

1. Introduction

The PK-4 system is the latest generation in the line of microgravity dusty plasma experiments currently in operation on board the International Space Station. Since its installation in the Columbus module in 2014, the PK-4 experiment has produced remarkable experimental data related to dust-particle-enhanced plasma emission (Usachev *et al.* 2016, 2018), transverse ionization instability (Zobnin *et al.* 2016), transformations of dust structures (Polyakov, Shumova & Vasilyak 2017), electrorheological and demixing phenomena (Dietz *et al.* 2017), particle kinetics (Liu *et al.* 2018), structural phase transitions (Dietz *et al.* 2018) and dust density waves (Jaiswal *et al.* 2018). Detailed reviews of past and recent microgravity dusty plasma activities can be found in Dietz *et al.* (2018) and Thomas *et al.* (2019).

Besides these fundamental physical investigations, analysis of the raw experimental data has shown that under some circumstances the dust particles show a tendency for chain formation where the particles align into lines several tens of particles long parallel to the discharge tube axis, as reported in Pustylnik *et al.* (2016) and Schwabe *et al.* (2019) and shown in figure 1. This happens most often (but not exclusively) when polarity switching is applied, in which the positive and negative polarities of direct current (DC) electrodes are alternated at a frequency of typically 100–500 Hz, with the aim of stabilizing the dust cloud in the field of view of the observing cameras.

Several previous experiments have produced structures with aligned grains. Dust lane formation has been reported, for example, during phase separation in binary complex plasmas under microgravity (Sütterlin *et al.* 2009; Du *et al.* 2012), driven by the electrostatic interaction between the charged dust grains in relative motion. Vertical dust particle chains can routinely be prepared in the electrode sheath region of a radio-frequency gas discharge (Kong *et al.* 2011, 2014; Chen *et al.* 2016), where particle alignment is stabilized by the enhanced horizontal confinement provided by an open glass box and the ion wake field due to the fast (supersonic) streaming of ions around the particles (Hutchinson 2011, 2012; Kompaneets, Morfill & Ivlev 2016). The electrorheological effect (or the homogeneous-to-string transition) can also favour dust chain formation as demonstrated by Ivlev *et al.* (2008, 2011). In this case the dust particles are surrounded by the quasi-neutral plasma bulk, but due to an externally applied alternating electric field and consequently streaming (subsonic) ions, the Debye screening sphere around the dust particles becomes distorted leading to an anisotropic interparticle repulsion. Note that this is different from the electrorheological effect in granular suspensions, which results from polarization of the grains themselves (Kwon, Piao & Choi 2015).

Among these known chain-forming processes, the electrorheological effect is the most probable one to be acting in the positive column region of the PK-4 discharge plasma. For a PK-4 neon discharge at $p = 50\,\mathrm{Pa}$ and $I = 1\,\mathrm{mA}$, the experimentally determined plasma parameters yield an axial electric field $E_z \simeq 2.2 \pm 0.2\,\mathrm{V\,cm^{-1}}$, with an electron density $n_e \simeq (2.2 \pm 0.2) \times 10^8\,\mathrm{cm^{-3}}$ and electron temperature $T_e \simeq 7 \pm 0.5\,\mathrm{eV}$ (Usachev *et al.* 2004; Khrapak *et al.* 2012). Assuming a stable positive column and based on the well-studied equilibrium transport behaviour of Ne^+ ions in neutral neon gas (Skullerud & Larsen 1990), one can estimate the ion drift velocity to be $v_{\mathrm{id}} \simeq 190\,\mathrm{m\,s^{-1}}$ resulting in a thermal Mach number $M_{\mathrm{th}} = v_{\mathrm{id}}/v_{\mathrm{th}} = 0.54$. Here the ion thermal velocity is defined as $v_{\mathrm{th}} = \sqrt{k_B T_i/m_i}$ assuming a temperature of $T_i = 300\,\mathrm{K}$ for the neon ions. The thermal Mach number is the key quantity for the estimation of the strength of the electrorheological effect based on the formula derived in Ivlev *et al.* (2008) for the pairwise interparticle

https://doi.org/10.1017/S0022377821001215 Published online by Cambridge University Press

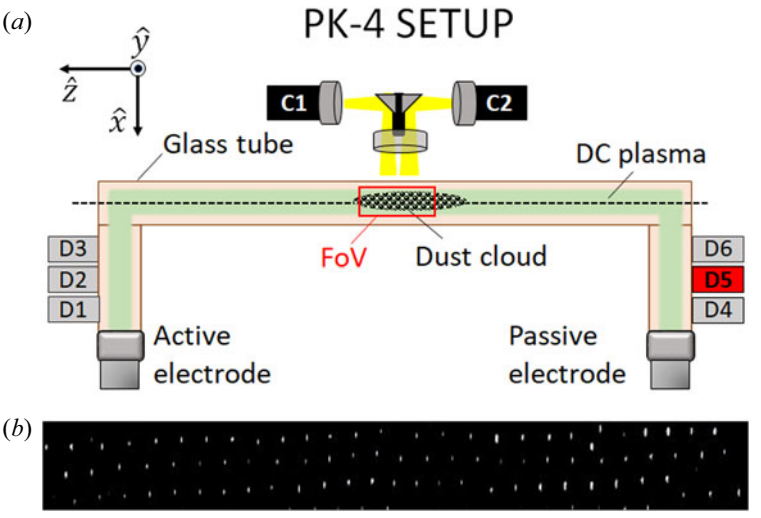

FIGURE 1. Top: schematic of the PK-4 experiment. Six microparticle dispensers (D1–D6) are mounted on the sides. Cameras C1 and C2 each have a field of view of $22.4 \times 16.8\,\mathrm{mm}^2$ and can be moved along as well as across the plasma chamber axis. Bottom: dust particles within the PK-4 experiment showing the formation of chains.

interaction energy:

$$W(r,\theta) \simeq \frac{Q^2}{4\pi\varepsilon_0}\left[\frac{\mathrm{e}^{-r/\lambda_D}}{r} - 0.43\frac{M_{\mathrm{th}}^2\lambda_D^2}{r^3}\left(3\cos^2\theta - 1\right)\right], \tag{1.1}$$

where r is the distance between two dust grains of charge Q aligned in the direction of the ion flow, θ is the angle relative to the ion drift direction and λ_D is the unperturbed Debye screening length. In this description the isotropic Yukawa (screened Coulomb) interaction is modified by a dipole-like term and higher-order contributions are neglected. It has been shown in Ivlev *et al.* (2008) that anisotropy in the particle distribution gradually starts to develop above a critical value of the thermal Mach number $M_{\mathrm{cr}} \simeq 0.3$ depending on the plasma conditions and that apparent ordered chains build up at $M_{\mathrm{th}} > 1$ with increasing length and stability as the ion drift speed is further increased. Based on these previous findings and the assumption of a stable DC positive column, it could be expected that given the typical PK-4 conditions discussed above, the estimated thermal Mach number of 0.54 is insufficient to result in the formation of long particle chains, in contrast with the observed particle behaviour. However, recent simulations and experiments have shown that the plasma column supports fast-moving ionization waves, with associated ion flows speeds $M_{\mathrm{th}} > 1$. Although these variations in the plasma occur on the microsecond time scale, they appear to have an influence on the dynamics of the dust grains, which typically occur on a millisecond time scale.

In this work, we examine conditions affecting dust chain structure formation in the PK-4 experiment based on realistic gas discharge modelling, dust particle charging simulations and calculations of the dust–dust and dust–ion interactions. Of particular interest is the strong electric field created by ionization waves which travel through the discharge column with a period on a microsecond time scale. A description of the PK-4 experiment and plasma conditions determined using a numerical model of the gas discharge are given in § 2, with a description of the molecular dynamics model of the ion and dust dynamics

https://doi.org/10.1017/S0022377821001215 Published online by Cambridge University Press

in § 3. The dust charge and configuration resulting from applying different time-averaged discharge conditions are given in § 4. These results are compared with observations from the PK-4 experiment in § 5. Concluding remarks are given in § 6.

2. Methods

The PK-4 experiment utilizes a long DC discharge with an active length of approximately 400 mm in a glass tube with inner diameter of 30 mm, equipped with both neon and argon gases (Pustylnik *et al.* 2016). The experiment utilizes several tools for manipulation of the dust, including movable radio-frequency coils, a heating ring (thermal manipulator), an auxiliary internal ring electrode (electrical manipulation) and a 20 W continuous infrared laser (optical manipulation), which makes the system very versatile. The DC drive is realized with a high-voltage arbitrary waveform generator with a frequency bandwidth up to 3 kHz, needed for applying polarity switching to the electrodes. Six dust particle dispensers are available, each filled with different monodisperse spherical dust grains made of melamine formaldehyde. In the experiment, the dust particles are suspended in the centre region of the discharge tube, in the bulk of the positive column. The observation of the dust ensemble and discharge glow is realized by video imaging, using a set of CCD cameras with an image resolution of 14.2 μm per pixel (Schwabe *et al.* 2019). A detailed description of the set-up and early experiments can be found in Pustylnik *et al.* (2016).

2.1. *Gas discharge modelling*

A cylindrical symmetric two-dimensional particle in cell with Monte Carlo collisions (PIC/MCC) code was implemented and used to simulate the motion and collisions of electrons and Ne^+ ions in neon gas and at solid surfaces in a DC discharge matching the PK-4 operating conditions. The electric field within the discharge tube is determined self-consistently from the boundary conditions at the electrodes and walls of the glass cylinder and the densities of the charged species. The simulation was used to determine the plasma characteristics within the PK-4 experiment for a DC plasma in neon held at a pressure of $p = 40$ Pa, gas temperature $T_g = 300$ K and discharge current $I = 0.8$ mA (with DC voltage of approximately 1000 V) with optional 500 Hz polarity switching. The model employed approximately 13×10^6 macroparticles for each of the species in the simulation on a 2048×64 simulation grid, closely matching the desired target of 100 particles/species per cell. A detailed description of the model, its implementation and experimental verification are presented in a separate publication (Hartmann *et al.* 2020).

Figure 2 shows the instantaneous spatial distribution (averaged over short time intervals of 250 ns in order to improve the signal-to-noise ratio) of selected plasma parameters. The global structure reproduces the traditional structure of long DC discharges: a short cathode fall with large electric field, followed by a low-field region with even a reversed field feature, and a small-field positive column down to the anode. A dominant feature of the instant global structure is the presence of ionization waves which develop on a microsecond time scale and travel along the column with phase velocities ranging between 500 and 1200 m s^{-1}. These quasi-periodic waves are characterized by a large-amplitude modulation of the charged particle densities (figure 2*a*,*b*) and alternating axial electric fields (figure 2*c*). A detailed analysis of the global plasma parameters computed with the same simulation under similar discharge conditions is presented in Hartmann *et al.* (2020). The time-averaged plasma parameters in the central region are $n_e = n_i = 2.1 \times 10^{14}$ m^{-3}, mean energies $\langle \epsilon \rangle_e = 4.4$ eV and $\langle \epsilon \rangle_i = 0.04$ eV and electric field $E = 245$ V m^{-1}. The presence of high-amplitude ionization waves along the positive column makes the time

https://doi.org/10.1017/S0022377821001215 Published online by Cambridge University Press

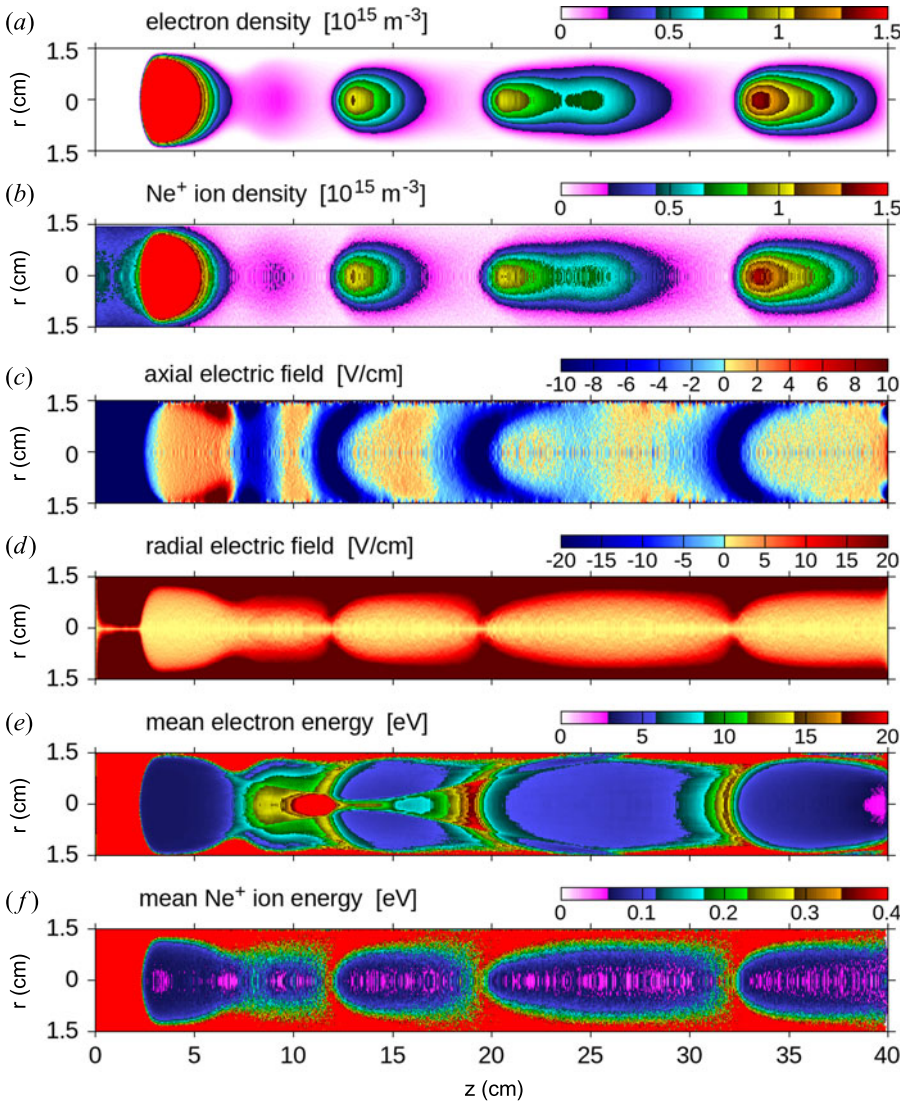

FIGURE 2. Computed spatial distributions of plasma parameters: electron density (*a*), Ne^+ ion density (*b*), axial electric field (where positive indicates in the direction of increasing z) (*c*), radial electric field (*d*), mean electron energy (*e*) and mean Ne^+ ion energy (*f*) at $p = 40$ Pa and $I = 0.8$ mA with the cathode at $z = 0$. The data acquisition time was set to a very short 0.25 μs. The real aspect ratio of 3 : 40 is scaled by stretching the radial axis by a factor of two for better visibility.

dependence of the plasma parameters at a given position (where the dust grains reside) of interest.

Here we focus on the local plasma environment in the central region of the discharge at position $z = 200$ mm and $r = 0$. In the following graphs the time dependence of the plasma parameters is shown with 0.25 μs resolution covering 250 μs total time at the central position of the cylinder. As shown in figure 2(*a*), the axial electric field varies in magnitude having a small positive value between the ionization waves (approximately

https://doi.org/10.1017/S0022377821001215 Published online by Cambridge University Press

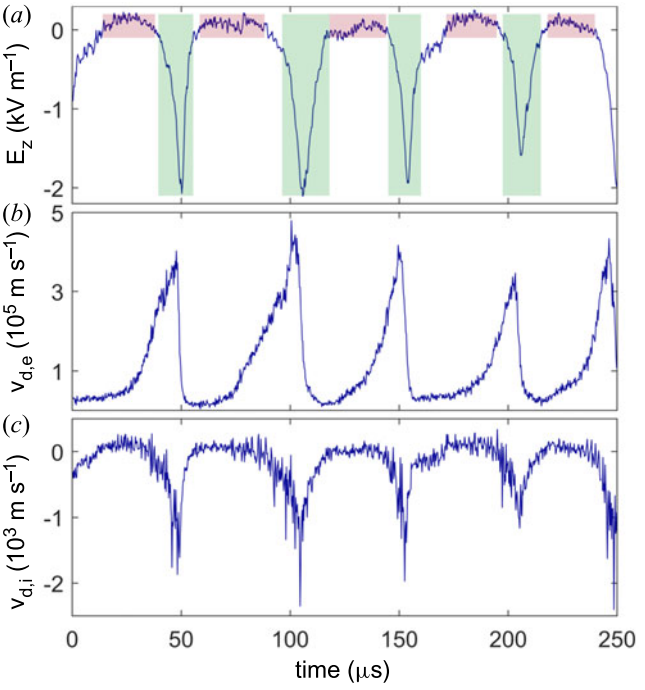

FIGURE 3. (*a*) Axial electric field at the centre of the column. Drift velocity of (*b*) electrons and (*c*) ions. The red shading indicates the times between the ionization waves, and the regions shaded in green denote the times when the electric field peaks within the ionization waves.

$100\,\mathrm{V\,m^{-1}}$, where positive indicates in the direction of increasing z) and peaking at approximately $-2000\,\mathrm{V\,m^{-1}}$ as an ionization front passes.

A similar structure is seen in the electron and ion velocities, which rapidly increase in magnitude within an ionization wave. The velocities are measured from the moments of the velocity distribution. The first moment is the average velocity, which shows the net mean drift velocity v_d imparted by the DC electric field in the column (figure 3*b*,*c*). The second moment of the velocity distribution gives the standard deviation, which is the average (thermal) velocity of the plasma particles, v_{th} (figure 4*a*,*b*). The temperatures calculated from the time-dependent thermal velocities,

$$T_{\mathrm{th}} = \frac{2mv_{\mathrm{th}}^2}{3k_B}, \tag{2.1}$$

are shown in figure 4(*c*,*d*). The fully time-averaged electron and ion thermal energies are $\langle\epsilon\rangle_e = 4.4\,\mathrm{eV}$ and $\langle\epsilon\rangle_i = 0.04\,\mathrm{eV}$. This is much greater than the average energies calculated between the ionization waves (marked by the shaded regions) $\langle\epsilon\rangle_e = 3.4\,\mathrm{eV}$ and $\langle\epsilon\rangle_i = 0.025\,\mathrm{eV} = 293\,\mathrm{K}$. Between the ionization waves, the ions thermalize with the neutral gas at temperature $T_n = 290\,\mathrm{K}$.

Note that the drift energy must be carefully taken into account in calculating the mean thermal energy. According to Monte Carlo simulations of ion drift in electric fields, the mean energy of the ions including the drift velocities is given by (Robertson & Sternovsky 2003)

$$\frac{1}{2}m_i\langle v_i^2\rangle = \frac{\pi}{4}m_i v_{d,i}^2 + \frac{3}{2}k_B T_n, \tag{2.2}$$

https://doi.org/10.1017/S0022377821001215 Published online by Cambridge University Press

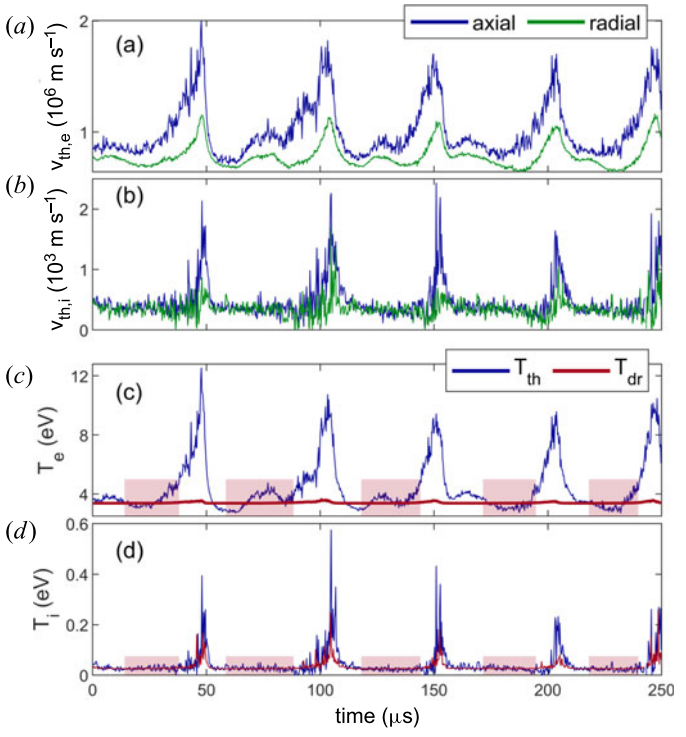

FIGURE 4. (*a*,*b*) Thermal velocities for the electrons and ions in the axial (blue) and radial (green) directions calculated from the standard deviation of the velocity distribution. The velocities in the tangential direction (not shown) are similar to those in the radial direction. (*c*,*d*) Temperature of the electrons and ions calculated from the thermal velocities, (2.1) (blue line), and the average temperature between ionization waves plus the drift energy, (2.3) (red line). The shaded areas indicate the times between the ionization waves when the ions thermalize with the neutral gas.

where T_n is the temperature of the neutral gas, leading to an expression for the ion temperature as a function of the drift velocity (Trottenberg, Block & Piel 2006):

$$T_{dr,i} = T_n + \left(\frac{\pi - 2}{6}\right)\frac{1}{k_B} m_i v_{dr,i}^2. \tag{2.3}$$

The ion temperature calculated in this manner is shown in figure 4(*d*) by the red line. Applying (2.3) gives an average ion temperature of $T_{dr,i} = 380\,\mathrm{K} = 0.033\,\mathrm{eV}$ over the full time interval, greater than that between the ionization waves, but less than that calculated without the drift correction. Using an equation similar to (2.3) to calculate the average electron energy shows that there is very little difference between the average electron energy between the ionization waves and that averaged over the full time interval, with $T_{dr,e} = 39\,543\,\mathrm{K} = 3.41\,\mathrm{eV}$ (as indicated by the red line in figure 4*c*).

Since the plasma variations occur on the microsecond time scale and the dust dynamics occurs on the millisecond time scale, it seems reasonable to use the time-averaged parameters to set the conditions used in the dust dynamics model. However, the drift velocity plays an important role in determining particle charge and the strength and extent of the ion wake. The ion drift velocity in this case is less than the sound speed of the plasma $c_s = \sqrt{k_v T_e/m_i}$. Given subsonic ion velocities, as the drift velocity increases the

https://doi.org/10.1017/S0022377821001215 Published online by Cambridge University Press

ion current to a grain's surface decreases, causing the grain to become more negatively charged. An increased charge causes the ions to be more strongly focused, resulting in a stronger ion wake. The increased flow velocity also causes the spatial extent of the ion wake to be narrower in the radial (cross-stream) direction and extended in the direction of ion flow (Matthews *et al.* 2019). The interparticle interaction energy, as given by (1.1), also depends on the ion flow velocity, predicting that anisotropy in the particle distribution begins to develop when $M_{\rm th} > 0.3$ (Ivlev *et al.* 2008, 2011). Between the striations, the average ion drift velocity is $v_{d,i} = 95\,{\rm m\,s^{-1}} = 0.22M_{\rm th}$. The average drift velocity over all times is $165\,{\rm m\,s^{-1}} = 0.39M_{\rm th}$, which would seem to be just great enough to start to induce anisotropy in the particle distribution. The average value within the ionization waves (times noted by the green boxes in figure 2) is $\langle v_{d,i}\rangle = 489\,{\rm m\,s^{-1}} = 1.14M_{\rm th}$, with an average peak value of $1951\,{\rm m\,s^{-1}} = 4.05M_{\rm th}$. Apparently, during the ionization waves the ion flow is great enough to cause a transition to strongly ordered strings. Accordingly, we are interested in investigating the effect that the increased electric field has on the formation of ordered dust strings in the PK-4 experiment.

2.2. *Dust and ions simulation*

The plasma conditions shown in figures 2 and 3 are used to model the dynamics and charging of the dust in a flowing plasma using the molecular dynamics code DRIAD (Dynamic Response of Ions and Dust) (Matthews *et al.* 2019), which solves the equations of motion of the ions and dust on their individual time scales. Here we compare the dust dynamics given the time-averaged plasma conditions (Case 1) with three cases where the electron and ion temperatures are set by the temperatures between the ionization waves (denoted by the red shaded regions in figure 3), but the electric field is increased to yield different values of the ion drift speed, $M_{\rm th} = v_{dr,i}/v_{\rm th}$. In Case 2, the average axial electric field without the ionization waves present is used (denoted by the red shaded regions in figures 3 and 4). In Case 3, the electric field averaged over the ionization waves (as indicated by the green boxes in figure 3) is applied. In Case 4, the magnitude of the electric field is set by the average of the half-maximum of the electric field in the ionization waves. In all cases, the polarity switching of the DC electric field is set to 500 Hz with a 50 % duty cycle (modelling symmetric switching of the electrode polarities) and the average plasma density is set to $n_e = n_i = 2.1 \times 10^{14}\,{\rm m^{-3}}$. The electron and ion temperatures, time-varying axial electric field $\tilde{E}$ and resultant time-varying ion drift velocity $\tilde{v}_{dr,i}$ for each case are given in table 1.

3. Dynamics of ions and dust

In each case, we simulate the motion of 20 dust grains (melamine formaldehyde) with radius $a = 3.43\,\mu{\rm m}$, which corresponds to dust particle size available in the PK-4 experiment. The dust particles are initially placed in a cloud near the centre of the simulation region, which has a radius of $1.5\lambda_e$ and length of $12\lambda_e$, where $\lambda_e = 940\,\mu{\rm m}$ is the electron Debye length of the plasma calculated for Cases 2–4. The equation of motion for dust grains with mass m_d and charge Q_d is given by

$$m_d \frac{{\rm d}\boldsymbol{v}_d}{{\rm d}t} = \boldsymbol{F}_{dd} + \boldsymbol{F}_{id} + Q_d\tilde{\boldsymbol{E}} + \nu^2 Q_d r\hat{r} - \beta\boldsymbol{v} + \zeta(t). \tag{3.1}$$

The forces between the dust particles $\boldsymbol{F}_{dd}$ are Coulomb interactions, as the ions in the simulation provide the shielding, while the forces between the dust and ions $\boldsymbol{F}_{id}$ are taken to be Yukawa interactions (Matthews *et al.* 2019; Ashrafi *et al.* 2020). The ion–dust interactions are accumulated over the elapsed ion time steps and then averaged

https://doi.org/10.1017/S0022377821001215 Published online by Cambridge University Press

Case	1	2	3	4
T_e (eV, K)	3.41, 39 500	3.38, 39 200	3.38, 39 200	3.38, 39 200
T_i (eV, K)	0.033, 380	0.025, 290	0.025, 290	0.025, 290
$v_{\mathrm{th},i}$ (m s^{-1})	489	424	424	424
$\tilde{E}$ (V m^{-1})	245	100	510	1000
$\tilde{v}_{dr,i}$ (m s^{-1})	165	93	429	719
M_{th}	0.34	0.22	1.01	1.69
$\langle Q_d \rangle$ (e^-)	3898	3667	4191	4819
Δ (μm)	396	392	401	402
$\langle r \rangle$ (μm)	14.5	12.6	11.6	11.9
$\langle r \rangle / \Delta$ (%)	3.6	3.2	2.9	3.0

TABLE 1. Discharge conditions used in the ion and dust simulation and calculated dust charge, interparticle spacing within the chain and average radial displacement.

before calculating the dust acceleration. The electric field $\tilde{E}$ is the axial electric field in the DC plasma which switches direction with the polarity switching frequency. There is a very strong confining force to keep the particles from the ends of the simulation region where the ions are injected (the ions need to travel approximately one Debye length to reach their equilibrium distribution). The parabolic radial confinement potential approximates the electric field from surrounding chains of charged dust particles where the confining strength $\nu^2 \propto \bar{Q}/(4\pi\epsilon_0\Delta^3)$, $\bar{Q}$ and Δ are the average expected particle charge and particle separation, and a constant of proportionality is used to account for the fact that there are multiple chains providing the confinement. Depending on the number of nearest neighbours assumed to participate in the confinement and the shielding length of the interaction potential, this constant of proportionality can range from $C = 0.5$ to 4.5. Dust density wave experiments performed in the PK-4 experiment in neon gas at 40 Pa found an estimated particle charge of $Z_d \approx 2200$ for $a = 1.60\,\mu$m particles (Jaiswal *et al.* 2018); assuming the charge scales linearly with the dust radius, the charge on a particle with radius $a = 3.43\,\mu$m is estimated to be $Z_d \approx 4500$. The average interparticle spacing, estimated from the number of particles visible in an image frame from the PK-4 experiment, is $\Delta \approx 305\,\mu$m. In all four cases simulated here, a fixed value of $\nu^2 = 3.0\bar{Q}/(4\pi\epsilon_0\Delta^3) = 6.8 \times 10^5\,\mathrm{V\,m^{-2}}$ was used. The neutral gas (density n_g and molecular mass m_g) provides both an energy sink and source with the neutral gas drag depending on the drag coefficient $\beta = (4\pi/3)\delta a^2 n_g m_g \sqrt{8k_B T_g/\pi m_g}$ (where δ is a material-dependent constant in the range 1.0–1.44; here we used 1.44 to represent diffuse reflection with accommodation of gas molecules from a non-conductor) and a Langevin thermostat set by $\zeta = \sqrt{2\beta k_B T_g/\Delta t_d}$ (the dust time step $\Delta t_d = 0.1$ ms). The system is allowed to evolve for 1.8 s, at which time the dust particles have reached their equilibrium configuration.

The wake-field interactions are included self-consistently by solving the equations of motion for the ions:

$$m_d \frac{\mathrm{d}\boldsymbol{v}_i}{\mathrm{d}t} = q_i \boldsymbol{E} + \boldsymbol{F}_{ii} + \boldsymbol{F}_{id}, \tag{3.2}$$

where the electric field consists of the confining electric field found within a cylindrical cavity within a homogeneous distribution of background ions, as well as the electric field in the DC plasma with polarity switching, $\tilde{E}$. The ion–ion interactions $\boldsymbol{F}_{ii}$ are derived from a Yukawa potential where the shielding is provided by the electrons,

https://doi.org/10.1017/S0022377821001215 Published online by Cambridge University Press

whereas the force between the ions and dust $\boldsymbol{F}_{id}$ is taken to be Coulombic in nature. This asymmetric treatment of the dust–ion forces has been shown to give a reasonable quantitative agreement for the potential distribution and interparticle forces (Piel 2017). The ions reach equilibrium on a time scale comparable to the ion plasma period $2\pi/\omega_i = 2\pi/\sqrt{n_i e^2/\epsilon_0 m_i} = 1.5 \times 10^{-6}$ s, which is fast compared with the period of the polarity switching, 2 ms. The effects of ion–neutral collisions are incorporated using the null collision method (Donkó 2011).

The charge on the dust grains is calculated self-consistently within the plasma wake field by summing the ion collisions over the elapsed ion time steps to determine the ion current. The electron velocity distribution in the PIC/MCC simulation varies on the same time scale as the ionization waves (0.05 ms peak-to-peak). Results from PIC/MCC simulation show that the second moment of the electron velocity distribution function indicates that coupling between the axial, tangential and radial velocity components and isotropization occurs on the sub-microsecond time scale (Hartmann *et al.* 2020). Both of these processes are fast compared to the dust charging time scale of several ion plasma periods. Thus the electrons are assumed to have a Boltzmann distribution and the electron current is set using orbital-motion-limited theory.

4. Results

The dust grain charging time is of the order of several ion plasma frequency periods, after which time the dust grains continue to undergo discrete stochastic charging with charge values fluctuating by ± 100 elementary charges from the equilibrium value. The resulting equilibrium dust charge and spatial configuration of the dust are shown for the four cases in figure 5. The view shown is a projection into the xz plane, with the radial scale magnified to show the relative displacement from the central axis. The ion–gas collisions cause the negative charge of the particles in the chains (indicated by the marker colour) to be reduced from that predicted by orbital-motion-limited theory, but the negative charge state increases with the ion drift speed, as expected.

The degree of order in the chain is evaluated using the linear pair correlation function $g(r)$, which was calculated at each dust time step and then averaged over the last 5000 time steps (0.5 s). The results are shown in figure 6. In general, the order within the chain increases as the electric field is increased (Cases 2–4). Case 2 (figure 6*b*) shows very little order beyond the third peak. This is a clear indication that the enhanced wakes due to the strong ion flow in the ionization waves contribute to the formation of ordered chains. The fully time-averaged condition, Case 1 (figure 6*a*), leads to a configuration which is more ordered than the thermal plasma without ionization waves (Case 2), but less ordered than the other two cases. Interestingly, the case with the highest degree of order is not that with the greatest electric field and resultant ion flow, but Case 3 (figure 6*c*), which employs the electric field averaged over the ionization waves.

Some clues to this order can be found by examining the ion density at equilibrium and the overall electric potential of the system. In figures 7 and 8, the ion density and the electric potential are shown for a slice in the xz plane. As shown in figure 7, each dust particle attracts a cloud of ions. In Cases 1 and 2 with the averaged plasma conditions, a distinct ion cloud surrounds each particle. As the electric field is increased in Cases 3 and 4, the ion cloud becomes elongated in the axial direction and the cloud around a grain begins to merge with that of neighbouring grains. The increased particle charge, in addition to the increased ion flow speed, concentrates the ions in a high-density ridge along the dust string.

https://doi.org/10.1017/S0022377821001215 Published online by Cambridge University Press

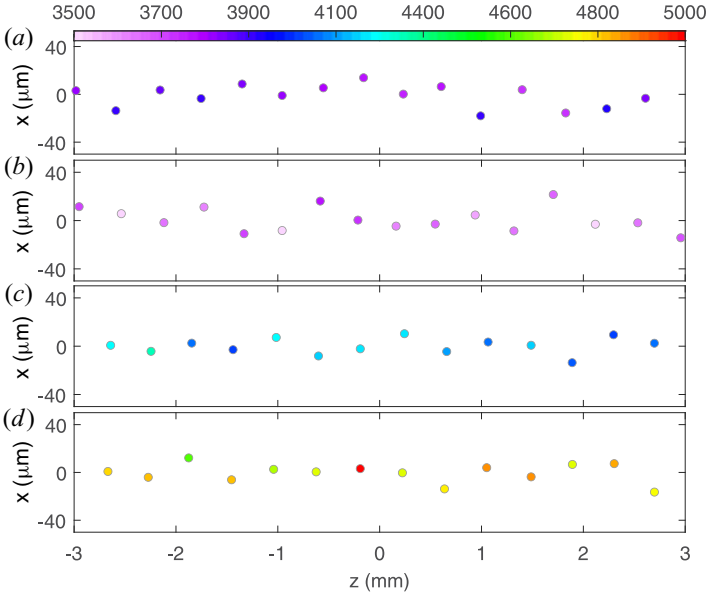

FIGURE 5. Final equilibrium charge and dust configuration for each case. Note that the scale in x is magnified to show the displacement from the central axis. The colour bar indicates the charge in units of elementary charge e^-. (*a*) Case 1; $\langle Q_d \rangle = 3900e^-$. (*b*) Case 2; $\langle Q_d \rangle = 3670e^-$. (*c*) Case 3; $\langle Q_d \rangle = 4190e^-$. (*d*) Case 4; $\langle Q_d \rangle = 4820e^-$.

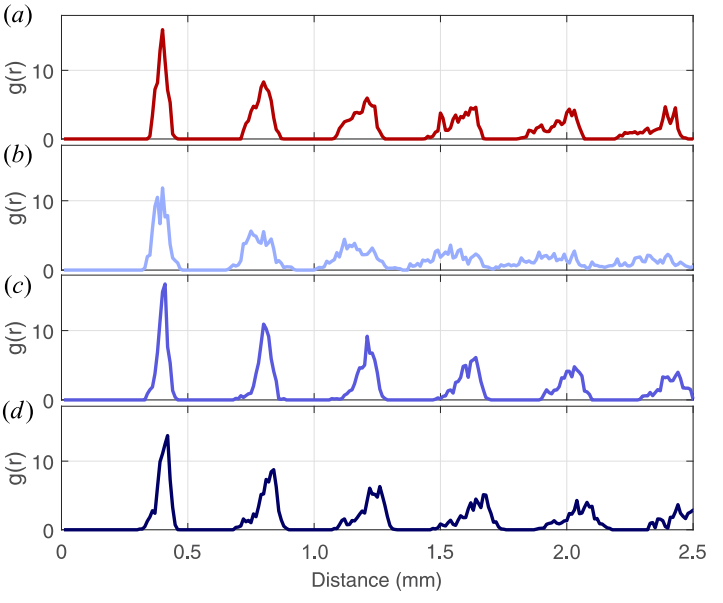

FIGURE 6. Pair correlation functions averaged over 0.5 s for each case. (*a*) Case 1; $\langle Q_d \rangle = 3900e^-$. (*b*) Case 2; $\langle Q_d \rangle = 3670e^-$. (*c*) Case 3; $\langle Q_d \rangle = 4190e^-$. (*d*) Case 4; $\langle Q_d \rangle = 4820e^-$.

https://doi.org/10.1017/S0022377821001215 Published online by Cambridge University Press

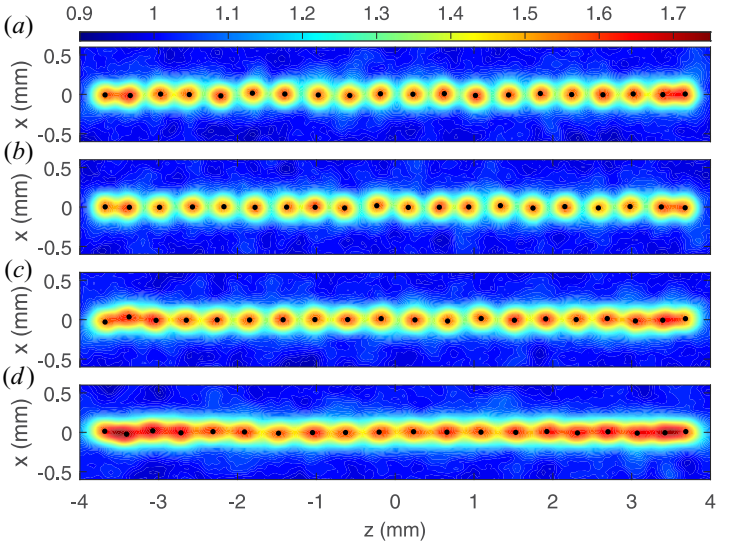

FIGURE 7. Final equilibrium ion density, where the colourbar indicates the density in units of the background density n_i/n_{i0}, $n_{i0} = 2.1 \times 10^{14}\,\mathrm{m}^{-3}$. The ion densities are shown for a slice through the xz plane averaged over 20 polarity cycles (40 ms). (*a*) Case 1, (*b*) Case 2, (*c*) Case 3 and (*d*) Case 4.

Finally, the combined electric potential from the ions and dust is shown at equilibrium in figure 8. Note that these figures are zoomed in on the central portion of the chain. The potentials are averaged over 20 polarity cycles (0.04 s). The colourbar indicates variations in potential in millivolts as the electric potential due to a dust grain with a charge of $4000e^-$ at a distance of 0.15 mm from the grain surface (approximately midway between adjacent dust grains) is approximately -0.038 V and the variation in potential due to the ion wakes is of the order of 0.01 V. The potential is measured with respect to the maximum potential just upstream/downstream of the dust string at $z \approx \pm 4$ mm. Profiles of the total potential along the axial direction are compared in figure 9 just above the dust string (in the radial direction) at $x = 0.2$ mm (figure 9*a*) and along the centre of the dust chain at $x = 0.0$ mm (figure 9*b*). Note that in Cases 1 and 2 the overall potential is dominated by the dust grains and is negative over much of the region surrounding the string. In Case 3, the potential is slightly positive just to the outside of the dust chain. In Case 4, an alternating positive/negative potential structure starts to emerge along the length of the chain. Although Cases 1 and 2 have the greatest disorder and displacement from the central axis of the chain, no correlation is found between the radial displacement of dust grains (which is on average $\approx 2\,\%$ of the interparticle spacing) and the height of the positive peaks.

5. Discussion

It is expected that the radial confinement should be proportional to Q_d^2, assuming that the radial confinement is due to the interaction between neighbouring strings. As given in (3.1), the magnitude of the radial confining force is $\nu^2 Q_d r$. For simplicity, the constant ν^2 was set to be $6.8 \times 10^5\,\mathrm{V\,m^{-2}}$ for all of the cases, resulting in a restoring force which is proportional to Q_d. Thus the radial restoring force used can be considered to be underpredicted for Cases 3 and 4 and overpredicted for Case 2, relative to Case 1. The average radial position of all the particles in each chain as a function of time is

https://doi.org/10.1017/S0022377821001215 Published online by Cambridge University Press

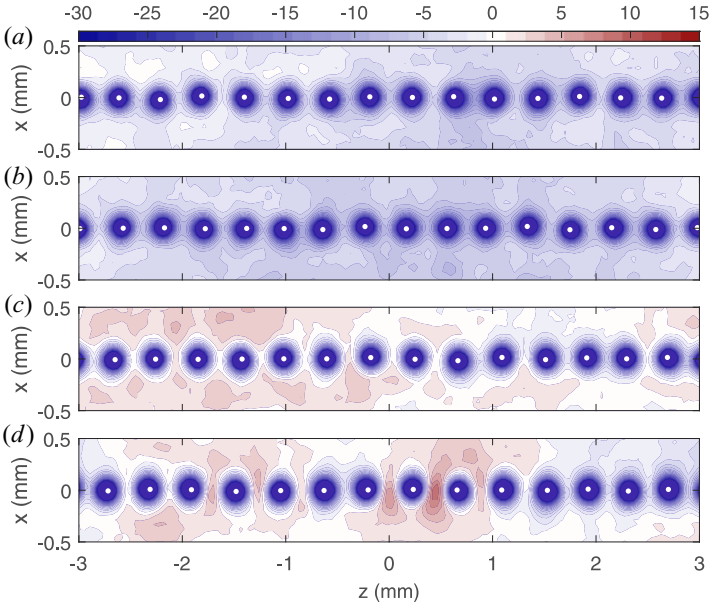

FIGURE 8. Equilibrium electric potential, where the colourbar indicates the difference from the maximum positive potential upstream/downstream of the strings in millivolts. The potentials are shown for a slice through the xz plane averaged over 20 polarity cycles (40 ms). (*a*) Case 1, (*b*) Case 2, (*c*) Case 3 and (*d*) Case 4.

shown in figure 10. After the initial Coulomb expansion of the dust cloud at the beginning of the simulation, the particles all settle near the z axis. As expected, the case with the largest average particle charge (Case 4) experiences the greatest radial restoring force and reaches the equilibrium radial position most quickly, followed by the other cases in order of decreasing average particle charge. However, even though the particles in Cases 3 and 4 have the greatest average charge, these chains have the smallest average radial displacement, representing better string structure. Notably, Case 1, with the time-averaged plasma conditions, has the greatest average radial displacement. This is a clear indication that the ion focusing produced by the strong axial electric field in Cases 3 and 4 allows for a smaller interparticle spacing within the string, despite the increased particle charge, and enhances string alignment.

For comparison, data from Campaign 4 of the PK-4 experiment performed in February 2017 are shown in figure 11(*a*) showing chains consisting of particles of 6.86 μm in diameter which were observed in neon gas at 45 Pa. The particles were trapped by the polarity-switched discharge (current of 1.0 mA and frequency of 500 Hz) with a duty cycle of 0.72, in order to compensate for the residual gas flow. A duty cycle of 0.72 corresponds to an asymmetric alternating current mode with 72 % of the cycle at positive voltage and 28 % at negative voltage. The linear pair correlation functions for five different chains (marked by the different symbols) were calculated and averaged over 70 frames (1.0 s) as shown in figure 11(*b*). Qualitatively, the pair correlation functions most closely resemble that shown for Case 3 (figure 6*c*) in that there are distinct, separate peaks out to the position of the sixth-nearest neighbour. The average interparticle spacing for the five chains is $\Delta = 270, 282, 281, 270, 277$ μm, from top to bottom, respectively, calculated from the first peak in $g(r)$. The average radial displacements of a chain's particles, measured as the perpendicular distance from a linear fit to the positions of the particles in a chain, are

https://doi.org/10.1017/S0022377821001215 Published online by Cambridge University Press

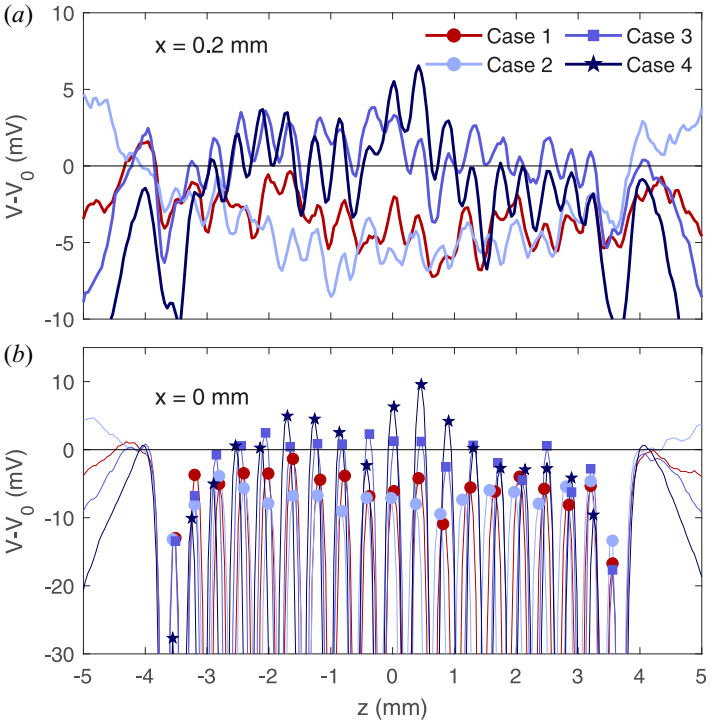

FIGURE 9. Equilibrium electric potential along the axial direction averaged over 20 polarity cycles (40 ms). (*a*) The profile just outside the dust string along $x = 0.2$ mm. (*b*) The profile along the centre of the dust string at $x = 0.0$ mm. The maximum positive potential between the dust grains is marked with symbols for each of the four cases.

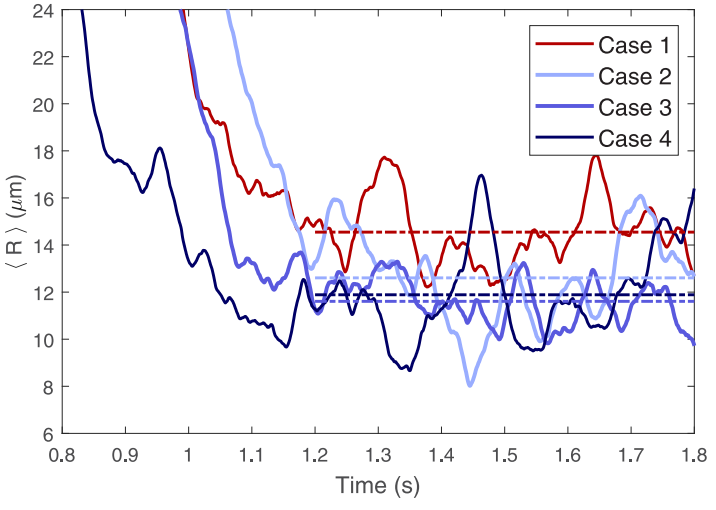

FIGURE 10. Average radial displacement of particles in the numerical simulation. The dashed lines indicate the average radial displacement over the last 0.6 s, after all of the particles have reached their equilibrium configuration. At equilibrium, the average radial displacements are 14.5 , 12.6 , 11.6 and 11.9 μm for Cases 1–4, respectively.

https://doi.org/10.1017/S0022377821001215 Published online by Cambridge University Press

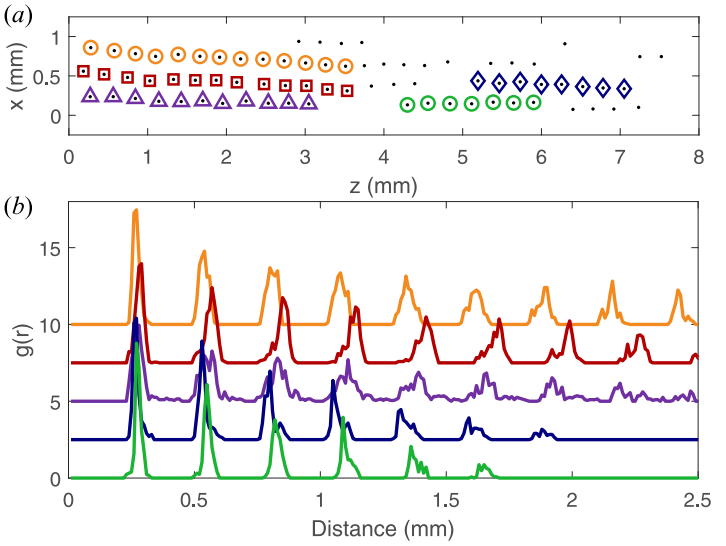

FIGURE 11. (*a*) Chains of dust particles observed in the PK-4 experiment. Symbols mark particles in five different chains which remained intact over the full time period. (*b*) Linear pair correlation function for each chain marked in (*a*), averaged over 70 frames (1.0 s). Each line is successively offset by 2.5 for clarity.

$\langle r \rangle = 11.6, 20.4, 16.8, 13.2, 17.8\,\mu$m. In the experiment, the average interparticle spacing within the chain is smaller, and average radial displacement is larger, than that found for the four cases in the numerical model (see table 1), such that $\langle r \rangle / \Delta = 4.3$, 7.2, 6.0, 4.9, 6.4 % for each chain, respectively. This suggests that the particle charge in the experiment may be less than estimated in the numerical model, possibly due to the fact that the dust density is great enough to deplete the electrons in the vicinity of the dust cloud. This would result in stronger ion wake potentials along the chain axis and weaker repulsion between neighbouring chains, allowing the particles more freedom for radial displacements. Another possible explanation for the observed larger average radial displacement of the dust particles in the experiment, as compared with the simulation, is that the asymmetric duty cycle used in the experiment led to asymmetric ion focusing around the dust grains. This could produce a stronger positive wake on one side of the dust, allowing smaller intrachain particle spacing, while weakening the radial restoring force and resulting in less stable chains.

One might also expect disorder in the chains to be correlated with the dust temperature, with dust grains which are more rigidly confined exhibiting more order and lower dust kinetic temperatures compared with unconstrained dust grains. This is actually not the case. The dust kinetic temperature was calculated from the velocities of the dust grains over the last 0.5 s of the simulation using $T_d = m_d \langle v^2 \rangle / 3k_b$. The mean dust temperatures were found to be $T_d = 862$ K (Case 1), 757 K (Case 2), 803 K (Case 3) and 1770 K (Case 4). The lowest dust kinetic temperature is found for Case 2, which exhibits the lowest average dust charge (and the largest amount of disorder), while the highest average temperature is found for Case 4 with the greatest charge (and a high degree of order). The current investigation shows that the dust kinetic temperature instead seems to be positively correlated with the electric field strength and thus the dust charge. This can be understood from a stronger confining force resulting in larger velocities as a particle oscillates about its equilibrium position. Note that the average dust temperature has contributions from

https://doi.org/10.1017/S0022377821001215 Published online by Cambridge University Press

both the diffusive motion due to random collisions with gas atoms/ions, which is related to the gas temperature, as well as the restoring force within the chain. The increased dust temperature for Case 1 (relative to Case 2) is therefore most likely due to the higher ion/gas temperature in this case.

6. Conclusion

A simulation of dust dynamics within a DC discharge plasma was used to investigate the role of strong electric fields created by ionization waves in the formation of chain-like dust structures within the plasma. A PIC/MCC code was used to determine the plasma conditions within the discharge tube, which were used to set the initial conditions and boundary conditions for an N-body simulation resolving the motion of the ions and the dust. The PIC/MCC simulation revealed that there are very strong variations in the plasma conditions on the microsecond scale which result in a large axial electric field with a peak magnitude of approximately $2000\,\mathrm{V\,m^{-1}}$, approximately 20 times greater than the background value between the ionization waves. Simulations of dust charging and dynamics show that time-averaged plasma temperatures and axial electric field lead to a weakly ordered string structure, leading to the conclusion that the time-averaged conditions do not seem to fully capture the plasma conditions which lead to chain formation. However, simulations using the plasma temperatures and densities between the ionization waves with an applied axial electric field show that the order within the string increases with the electric field strength. The numerical results most closely resemble data from the PK-4 experiment when the average electric field during the ionization waves is applied. It appears that the enhanced electric field associated with the ionization waves could play an important role in generating the string-like structures observed in the PK-4 experiment.

These simulations were run assuming constant plasma conditions including electron and ion temperatures and number densities. Future work will examine the effect of time-varying plasma parameters calculated from the PIC/MCC simulation on the dust charging and dynamics.

Acknowledgements

All authors gratefully acknowledge the joint ESA–Roscosmos Experiment Plasmakristall-4 on board the International Space Station. The microgravity research is funded by the space administration of the Deutsches Zentrum für Luft- und Raumfahrt eV with funds from the Federal Ministry for Economy and Technology according to a resolution of the Deutscher Bundestag under grant nos. 50WM1441 and 50WM2044. A.M.L. and A.D.U. were supported by Russian Science Foundation grant no. 20-12-00365 and participated in the preparation of this experiment and its execution on board the International Space Station. L.S.M., T.W.H. and M.R. received support from NASA grant no. 1571701 (L.S.M. and T.W.H.) and NSF grant no. 1740203 (L.S.M., T.W.H. and M.R.) and the US Department of Energy, Office of Science, Office of Fusion Energy Sciences under award no. DE-SC-0021334 (L.S.M. and T.W.H.). P.H. gratefully acknowledges support from the Hungarian Research, Development and Innovation Office via grant K-134462.

Editor Edward Thomas, Jr thanks the referees for their advice in evaluating this article.

Declaration of interests

The authors report no conflict of interest.

REFERENCES

Ashrafi, K. S., Yousefi, R., Chen, M., Matthews, L. S. & Hyde, T. W. 2020 Dust as probes: determining confinement and interaction forces. *Phys. Rev.* E **102**, 043210.

Chen, M., Dropmann, M., Zhang, B., Matthews, L. S. & Hyde, T. W. 2016 Ion-wake field inside a glass box. *Phys. Rev.* E **94**, 033201.

Dietz, C., Bergert, R., Steinmüller, B., Kretschmer, M., Mitic, S. & Thoma, M. H. 2018 fcc-bcc phase transition in plasma crystals using time-resolved measurements. *Phys. Rev.* E **97**, 043203.

Dietz, C., Kretschmer, M., Steinmüller, B. & Thoma, M. 2017 Recent microgravity experiments with complex direct current plasmas. *Contrib. Plasma Phys*. **58** (1), 21–29.

Donkó, Z. 2011 Particle simulation methods for studies of low-pressure plasma sources. *Plasma Sources Sci. Technol*. **20**, 024001.

Du, C.-R., Sütterlin, K. R., Jiang, K., Räth, C., Ivlev, A. V., Khrapak, S., Schwabe, M., Thomas, H. M., Fortov, V. E., Lipaev, A. M., *et al.* 2012 Experimental investigation on lane formation in complex plasmas under microgravity conditions. *New J. Phys*. **14** (7), 073058.

Hartmann, P., Rosenberg, M., Juhasz, Z., Matthews, L. S., Sanford, D. L., Vermillion, K., Reyes, J. C. & Hyde, T. W. 2020 Ionization waves in the PK-4 direct current neon discharge. *Plasma Sources Sci. Technol*. **29** (11), 115014.

Hutchinson, I. H. 2011 Nonlinear collisionless plasma wakes of small particles. *Phys. Plasmas* **18** (3), 032111.

Hutchinson, I. H. 2012 Intergrain forces in low-mach-number plasma wakes. *Phys. Rev.* E **85**, 066409.

Ivlev, A. V., Morfill, G. E., Thomas, H. M., Räth, C., Joyce, G., Huber, P., Kompaneets, R., Fortov, V. E., Lipaev, A. M., Molotkov, V. I., *et al.* 2008 First observation of electrorheological plasmas. *Phys. Rev. Lett*. **100**, 095003.

Ivlev, A. V., Thoma, M. H., Räth, C., Joyce, G. & Morfill, G. E. 2011 Complex plasmas in external fields: The role of non-hamiltonian interactions. *Phys. Rev. Lett*. **106**, 155001.

Jaiswal, S., Pustylnik, M. Y., Zhdanov, S., Thomas, H. M., Lipaev, A. M., Usachev, A. D., Molotkov, V. I., Fortov, V. E., Thoma, M. H. & Novitskii, O. V. 2018 Dust density waves in a dc flowing complex plasma with discharge polarity reversal. *Phys. Plasmas* **25** (8), 083705.

Khrapak, S. A., Tolias, P., Ratynskaia, S., Chaudhuri, M., Zobnin, A., Usachev, A., Rau, C., Thoma, M. H., Petrov, O. F., Fortov, V. E., *et al.* 2012 Grain charging in an intermediately collisional plasma. *Europhys. Lett*. **97** (3), 35001.

Kompaneets, R., Morfill, G. E. & Ivlev, A. V. 2016 Wakes in complex plasmas: a self-consistent kinetic theory. *Phys. Rev.* E **93**, 063201.

Kong, J., Hyde, T. W., Matthews, L., Qiao, K., Zhang, Z. & Douglass, A. 2011 One-dimensional vertical dust strings in a glass box. *Phys. Rev.* E **84**, 016411.

Kong, J., Qiao, K., Matthews, L. S. & Hyde, T. W. 2014 Interaction force in a vertical dust chain inside a glass box. *Phys. Rev.* E **90**, 013107.

Kwon, S. H., Piao, S. H. & Choi, H. 2015 Electric field-responsive mesoporous suspensions: a review. *Nanomaterials* **5** (4), 2249–2267.

Liu, B., Goree, J., Pustylnik, M. Y., Thomas, H. M., Fortov, V. E., Lipaev, A. M., Usachev, A. D., Molotkov, V. I., Petrov, O. F. & Thoma, M. H. 2018 Particle velocity distribution in a three-dimensional dusty plasma under microgravity conditions. *AIP Conf. Proc*. **1925** (1), 020005.

Matthews, L. S., Sanford, D. S., Kostadinvoa, E., Ashrafi, K. S., Guay, E. & Hyde, T. W. 2019 Dust charging in dynamic ion wakes. *Phys. Plasmas* **27**, 023703.

Piel, A. 2017 Molecular dynamics simulations of ion flows around dust particles. *Phys. Plasmas* **24** (3), 033712.

Polyakov, D. N., Shumova, V. V. & Vasilyak, L. M. 2017 Transformations of dust structures in glow dc discharge in neon: effect of gas temperature and discharge current. *Plasma Sources Sci. Technol*. **26** (8), 08LT01.

Pustylnik, M. Y., Fink, M. A., Nosenko, V., Antonova, T., Hagl, T., Thomas, H. M., Zobnin, A. V., Lipaev, A. M., Usachev, A. D., Molotkov, V. I., *et al.* 2016 Plasmakristall-4: new

complex (dusty) plasma laboratory on board the international space station. *Rev. Sci. Instrum*. **87** (9), 093505.

ROBERTSON, S. & STERNOVSKY, Z. 2003 Monte Carlo model of ion mobility and diffusion for low and high electric fields. *Phys. Rev.* E **67**, 046405.

SCHWABE, M., RUBIN-ZUZIC, M., RÄTH, C. & PUSTYLNIK, M. 2019 Image registration with particles, examplified with the complex plasma laboratory pk-4 on board the international space station. *J. Imaging* **5** (3), 39.

SKULLERUD, H. R. & LARSEN, P. H. 1990 Mobility and diffusion of atomic helium and neon ions in their parent gases. *J. Phys.* B **23** (6), 1017.

SÜTTERLIN, K. R., WYSOCKI, A., IVLEV, A. V., RÄTH, C., THOMAS, H. M., RUBIN-ZUZIC, M., GOEDHEER, W. J., FORTOV, V. E., LIPAEV, A. M., MOLOTKOV, V. I., *et al.* 2009 Dynamics of lane formation in driven binary complex plasmas. *Phys. Rev. Lett*. **102**, 085003.

THOMAS, H. M., SCHWABE, M., PUSTYLNIK, M. Y., KNAPEK, C. A., MOLOTKOV, I. V., LIPAEV, A. M., PETROV, O. F., FORTOV, V. E. & KHRAPAK, S. A. 2019 Complex plasma research on the international space station. *Plasma Phys. Control. Fusion* **61** (1), 0.

TROTTENBERG, T., BLOCK, D. & PIEL, A. 2006 Dust confinement and dust-acoustic waves in weakly magnetized anodic plasmas. *Phys. Plasmas* **13**, 042105.

USACHEV, A., ZOBNIN, A., PETROV, O., FORTOV, V., THOMA, M., KRETSCHMER, M., RATYNSKAIA, S., QUINN, R., HOEFNER, H. & MORFILL, G. 2004 The project "Plasmakristall - 4" (PK-4) – a dusty plasma experiment in a combined dc/rf (i) discharge plasma under microgravity conditions. *Czech. J. Phys*. **54** (3), C639.

USACHEV, A. D., ZOBNIN, A. V., PETROV, O. F., FORTOV, V. E., THOMA, M. H., PUSTYLNIK, M. Y., FINK, M. A. & MORFILL, G. E. 2016 Elongated dust clouds in a uniform dc positive column of low pressure gas discharge. *Plasma Sources Sci. Technol*. **25** (3), 035009.

USACHEV, A. D., ZOBNIN, A. V., SHONENKOV, A. V., LIPAEV, A. M., MOLOTKOV, V. I., PETROV, O. F., FORTOV, V. E., PUSTYL'NIK, M. Y., FINK, M. A., THOMA, M. A., *et al.* 2018 Influence of dust particles on the neon spectral line intensities at the uniform positive column of dc discharge at the space apparatus "Plasma Kristall-4". *J. Phys.: Conf. Ser*. **946** (1), 012143.

ZOBNIN, A. V., USACHEV, A. D., LIPAEV, A. M., PETROV, O. F., FORTOV, V. E., PUSTYLNIK, M. Y., THOMAS, H. M., FINK, M. A., THOMA, M. H. & PADALKA, G. I. 2016 Transverse ionization instability of the elongated dust cloud in the gas discharge uniform positive column under microgravity conditions. *J. Phys.: Conf. Ser*. **774** (1), 012174.

https://doi.org/10.1017/S0022377821001215 Published online by Cambridge University Press